Colloids and Surfaces A: Physicochemical and Engineering Aspects 734 (2026) 139438

Contents lists available at ScienceDirect

Colloids and Surfaces A: Physicochemical and Engineering Aspects

journal homepage: www.elsevier.com/locate/colsurfa

Enhancing early osteogenic differentiation on Ti6Al4V implants via MAO coatings doped with strontium and calcium

Roman Gabor [a,1], Martina Doubkova [a,b,1], Ladislav Cvrcek [a,c], Elena Filova [a,b,*], Marina Malic [a,b], Karel Masek [a,d], Josef Hlinka [e], Grazyna Simha Martynkova [a], Jan Walter [c], Marek Vecer [f], Jana Seidlerova [a,g], Michaela Tokarcíkova [a], Lucie Bacakova [a,b]

[a] Nanotechnology Centre, CEET, VSB – Technical University of Ostrava, 17. listopadu 15/2172, Ostrava-Poruba 708 00, Czech Republic
[b] Laboratory of Biomaterials and Tissue Engineering, Institute of Physiology of the Czech Academy of Sciences, Prague 4 142 00, Czech Republic
[c] Department of Materials Engineering, Faculty of Mechanical Engineering, Czech Technical University in Prague, Karlovo náměstí 293/13, Prague 2 120 00, Czech Republic
[d] Department of Surface and Plasma Science, Faculty of Mathematics and Physics, Charles University, V Holešovičkách 2, Prague 8 18000, Czech Republic
[e] Department of Materials Engineering, Faculty of Materials Science and Technology, VSB-Technical University of Ostrava, 17. listopadu 2172/15, Ostrava-Poruba 708 00, Czech Republic
[f] Centre for Chemical Engineering, Faculty of Materials Science and Technology, VSB-Technical University of Ostrava, 17. listopadu 2172/15, Ostrava-Poruba 708 00, Czech Republic
[g] Department of Chemistry and Physico-Chemical Processes, Faculty of Materials Science and Technology, VSB-Technical University of Ostrava, 17. listopadu 2172/15, Ostrava-Poruba 708 00, Czech Republic

HIGHLIGHTS

- Oxide layers containing Sr or Sr+Ca were prepared on the Ti6Al4V alloy by MAO.
- Presence of Sr and Sr+Ca in oxide layer improved material corrosion resistance.
- Sr was released continuously from the oxide layers over 60 days.
- Sr or Sr+Ca layers evinced the highest coefficient of friction on polished alloy.
- Bioactive Sr- and Sr+Ca-doping improved osteogenic differentiation *in vitro*.

GRAPHICAL ABSTRACT

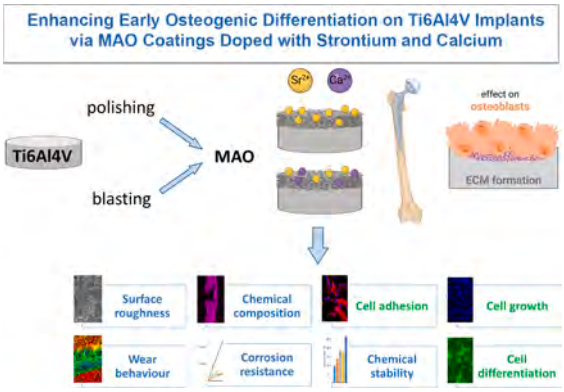

ARTICLE INFO

Keywords:
Osseointegration
MAO process

ABSTRACT

Titanium alloys such as Ti6Al4V are widely used in orthopaedic implants due to their excellent mechanical and corrosion-resistant properties. However, insufficient early-stage osseointegration remains a critical challenge, often leading to implant loosening and failure. To overcome this issue, bone implant design and surface

* Corresponding author at: Laboratory of Biomaterials and Tissue Engineering, Institute of Physiology of the Czech Academy of Sciences, Videnska 1083, Prague 4 142 00, Czech Republic.
E-mail address: elena.filova@fgu.cas.cz (E. Filova).
[1] Both authors contributed equally.

https://doi.org/10.1016/j.colsurfa.2025.139438
Received 2 October 2025; Received in revised form 24 December 2025; Accepted 30 December 2025
Available online 31 December 2025

Wear resistance
Corrosion behavior
Cell differentiation
Bioactive material

modification increasingly focus on incorporating bioactive elements. This study explores the enhancement of osseointegration through micro-arc oxidation (MAO) surface modification of Ti6Al4V, incorporating bioactive strontium (Sr) and calcium (Ca) ions. Two surface pretreatments — polishing (P) or shot-blasting (B) — were applied prior to MAO to generate coatings with distinct topographies and compositions: TAV(P), TAV(P)-Sr, TAV (P)-Sr-Ca, TAV(B), TAV(B)-Sr, and TAV(B)-Sr-Ca. Surface characterization of the resulting oxide layers confirmed the incorporation of Sr, Ca, and phosphate ions, with Sr releasing continuously over 60 days. Wear resistance analysis revealed the highest coefficient of friction for the TAV(P)-Sr coatings and the lowest values for TAV(B)-Sr. Surface modification by blasting led to reduced corrosion resistance in the TAV(B), TAV(B)-Sr, and TAV(B)-Sr-Ca samples. Nevertheless, enhanced corrosion resistance was observed in all samples modified with Sr and Sr+Ca. *In vitro* analyses using human bone marrow-derived mesenchymal stromal cells (hBMSCs) demonstrated excellent biocompatibility of all coatings. Notably, Sr-doped and especially Sr-Ca-doped surfaces significantly enhanced early osteogenic differentiation, as evidenced by increased alkaline phosphatase activity and type I collagen deposition. These findings highlight the synergistic effects of surface topography and Sr-Ca ion doping in promoting early-stage osseointegration, offering a promising strategy for improving the performance of titanium-based bone implants, particularly in patients with compromised bone healing.

1. Introduction

Titanium and Ti6Al4V alloy are frequently used for bone orthopaedic implants, as they have excellent corrosion properties, high biocompatibility and osseointegration with bone tissue [1]. However, there is an increase in the number of implant failures due to insufficient osseointegration with bone tissue, accompanied by loosening of implants at the interface with bone tissue that causes so-called micro-movements and the formation of a fibrous capsule. Other factors causing implant failure include the loading time, the type of implant, the material used and the size of the implant [2].

There is an effort to improve osseointegration of the implant with the bone tissue using various surface modifications of the implant material. For this purpose, the MAO method, which enables targeted functionalization of biomaterial surfaces, leading to proper surface microarchitecture and chemical composition, corrosion and mechanical properties, has found its place in industrial practice [3]. The mechanism of oxide layer development during MAO application involves a series of complex electrochemical, chemical and physical reactions that are not yet fully understood. The oxidation reactions occur at the anode in both acidic and alkaline electrolytes in the presence of additives (Ag, Cu, Zn, Sr, glycerol) that affect the resulting properties of the ceramic layers [4–6]. Applying increased voltage initiates a plasma discharge in a multi-step MAO process, which is accompanied by the development of an oxide layer and a decrease in the current flow. At the termination of the MAO process, electrolyte ions fill the channels of the growing oxide layer as the ions react together with the products of the ongoing oxidation reactions [7].

The development of optimal electrolyte compositions for MAO applications is moving towards the use of bioactive inorganic ions, such as biogenic calcium phosphates and strontium ions, which are bioactive, osteoconductive, osteoinductive and can enhance the osseointegration of bone implants.

Hydroxyapatite is a natural inorganic part of bone, present in nanosized, poorly crystalline and non-stoichiometric form; it contains CO_3, HPO_4, lattice vacancies and is deficient in Ca and OH [8]. Its composition can be expressed by the chemical formula (where Ø are vacancies): $Ca_{8.3}Ø_{1.7}(PO_4)_{4.3}(CO_3$ and $HPO_4)_{1.7}(OH$ and/or $½CO_3)_{0.3}Ø_{1.7}$. Bone apatite is able to accept many different ionic substitutions, i.e. Sr in its crystal structure. Strontium is an element naturally present in bone and tooth enamel in trace amounts. Sr incorporated in bone stimulates osteoblast proliferation, osteogenic differentiation and bone formation and inhibits bone resorption activity of osteoclasts through the activation of signaling pathways that play a role in cell survival, proliferation and differentiation [9,10]. These beneficial effects of Sr were also documented in a systematic study [11], which showed that incorporating Sr into the MAO coating of titanium implants significantly improved osseointegration and bone apposition on these implants in animal models. The proportion of Sr in ion-doped MAO coatings represents a potential future development of modified coatings in terms of their antioxidant properties and enhanced early osseointegration, especially in patients with osteoporosis [12]. Strontium-modified Ti-P-DA-Sr implants have demonstrated significantly improved early osseointegration in osteoporotic environments by promoting osteogenesis and simultaneously modulating the immune response towards the anti-inflammatory M2 phenotype. The study [13] shows that the combination of polydopamine coating and Sr ion release effectively stabilizes the bone-implant interface and represents a promising strategy for implants in patients with osteoporosis.

The topographical structure is another key parameter of their surface, which directly influences the behavior of stem cells, osteoblasts, osteoblast precursor cells, endothelial cells, and macrophages, as well as the process of osteogenesis at both micro- and nanoscale level. Osteogenesis represents the regulation of the functions of the mesenchymal stem cells (MSCs) and their differentiation into osteoblasts; however, under other conditions and stimuli, MSCs can also differentiate into adipocytes or chondrocytes. In terms of cell adhesion, migration and osteogenic differentiation, surface topography has a broad regulatory influence [14]. Increased surface topography at the micron-scale level has been shown to stimulate extracellular matrix synthesis of adherent cells and to accelerate the osseointegration process. An enhanced osseointegration effect of the micron-scale topography has been observed *in vivo* and was accepted in the case of a modified cpTitan surface for dental implants [15].

In the current study, the MAO technique was applied to Ti6Al4V samples in order to prepare two types of coatings with different contents of Sr, Ca and phosphate ions. In addition, Ti6Al4V samples with different topographies of surface, prepared by different mechanical methods, were studied in detail, either alone or in combination with the MAO modifications. The effect of the newly developed materials on cell adhesion, proliferation, metabolic activity, and osteogenic differentiation was assessed *in vitro* using cultures of mesenchymal stromal cells derived from human bone marrow (hBMSCs).

2. Materials and methods

2.1. Sample preparation

The surfaces of Ti6Al4V alloy samples (15 mm in diameter, 2.6 mm in thickness) were mechanically ground and polished using #400 and #1200 grit SiC paper, creating a TAV(P) sample. For selected groups of samples, the surfaces were subsequently treated using a shot-blasting system with an injector (GDS Technology s.r.o., Czech Republic) at a working distance of 50 mm and a pressure of 2 bar for 5 min, using synthetic Al_2O_3 with a grain size of up to 0.7 mm as the abrasive medium. These processes resulted in the creation of TAV(B) samples. The samples were then modified by MAO with the use of two different electrolytes under the conditions described below. The MAO technique

was used in a pulsed mode by applying a voltage of 450 V, a pulse size of 0.7 ms, a pulse gap size of 7 ms, and a time of 8 min. To study the effect of Sr and phosphates on the materials' properties, TAV(P)-Sr and TAV (B)-Sr samples were prepared under the MAO technique using an electrolyte containing 4 g/L SrOH, 6.0 g/L $C_{10}H_{14}N_2Na_2O_8{\cdot}2H_2O$ (EDTA), 16.0 g/L Na_3PO_4, 40 g/L CH_3COOH with conductivity 15.3 mS/cm, and pH 4.0 was used. To study the effect of Sr, phosphates and Ca on the materials' properties, TAV(P)-Sr-Ca and TAV(B)-Sr-Ca were prepared under MAO modification using an electrolyte containing 4 g/L SrOH, 6.0 g/L $C_{10}H_{14}N_2Na_2O_8{\cdot}2H_2O$ (EDTA), 16.0 g/L Na_3PO_4, 4.0 g/L $C_4H_6CaO_4$, 40 g/L CH_3COOH with conductivity of 17.9 mS/cm; pH 4.0 was used.

2.2. Surface analysis of coatings

The surface and cross-section of the samples were studied using a field-emission scanning electron microscope (FE-SEM, JEOL JSM-7610F Plus, JEOL, Japan) and a backscattered electron (BSE) detector with an attached energy-dispersive X-ray spectrometer (EDX, Oxford Instruments).

The chemical state of the MAO coatings was evaluated by X-ray photoelectron spectroscopy (XPS). The spectra were collected using a hemispherical analyzer equipped with a multichannel detector using Al Kα radiation sources. Surface roughness R_a (arithmetic average of the absolute values of the profile heights) and R_z (maximum height of the profile) measurements were carried out in contact mode on a profilometer device (Talysurf 50, Taylor Hobson).

The phase analysis of the samples was performed using the Rigaku Ultima IV diffractometer (Rigaku Corporation, Japan). The measurements were carried out under conditions of Cu K_α radiation utilization at an accelerating voltage of 40 kV, current of 40 mA, scanning rate of 1°/min and a scan range of 10–100°2θ. The phase composition was evaluated using the ICDD PDF-2 2022 database. The contact angle (CA) was measured using the optical tensiometer Theta Flex (Biolin Scientific, Sweden) and a simulated body fluid (SBF) [16].

2.3. Tribological analysis

The tribological properties were tested using a pin-on-disc CSM Instrument tribometer in rotational configuration. Al_2O_3 balls with a diameter of 6 mm were used as counter bodies. The samples and balls were cleaned with acetone prior to testing. The tests were performed in phosphate-buffered saline (PBS, Sigma-Aldrich, USA) to simulate the environment of the human body. The testing solution was composed of 10 mM phosphate buffer, 2.7 mM KCl and 137.0 mM NaCl and had a pH of 7.4 at 25 °C.

The normal load used during the test was 1 N, and the linear sliding speed was 50 mm.s^{-1} for each test. The number of laps was 5000 and the radius of the track was 5 mm. The friction coefficient μ was calculated from the ratio of the tangential friction force and the normal force. The surfaces of the Al_2O_3 ball and the wear track after testing were analyzed using the digital microscope Olympus DSX1000. The wear track profile was analyzed by Zygo NewView 7200. The specific wear rate k was calculated from the equation $k = V / F.s$, where V is the wear volume, F is the normal load, and s is the sliding distance. The wear volume was obtained by multiplying the area of the wear track cross-section and the wear track circumference.

An adhesion test was performed with the Revetest Scratch Xpress+ scratch tester (CSM Instruments, Switzerland). A Rockwell diamond tip (radius 200 μm) was used as an indenter. The scratch test load was set to increase linearly from 1 N to 30 N along the 3 mm scratch with a linear speed of 10 mm/min. The results of the tests were analyzed by DSX1000 digital optical microscopy (Olympus, Japan). Measurements were carried out on a pair of identical samples, always using a 5 mm radius.

2.4. Corrosion tests and ion release

The corrosion behavior of the samples was studied in a three-electrode system (Voltalab PGZ 100, France) equipped with Voltamaster 10 software. The samples were connected as working electrodes; a calomel electrode was used as a reference electrode, and a carbon rod was used as an auxiliary electrode. The samples were tested in an isotonic physiological solution (0.9 wt% NaCl in double-distilled H_2O) in order to simulate the environment of living tissue. The electrochemical impedance spectroscopy (EIS) method was used to determine the electrochemical parameters of the tested surface layers. Before starting the potentiodynamic polarisation, the initial potential value was set to −70 mV vs. the open circuit potential (OCP) after stabilisation of the corrosion equilibrium, with the polarisation rate set to 60 mV.min^{-1}.

The release of Sr from MAO coatings was determined by immersion testing. Samples were immersed in 50 ml of PBS solution (pH 7.4) and shaken in an intermittent rotation vessel (10 rpm) at laboratory temperature. From the mixtures, 10 ml of the solutions were taken at different intervals: 1, 7, 14, 28, 60 days. The total amount of Sr in MAO coatings was determined following the immersion test and their subsequent digestion in hot HCl solution (1:1). The Sr concentration was determined using an atomic emission spectrometer with inductively coupled plasma (AES-ICP), Spectro Arcos (SPECTRO Analytical Instruments Inc., Germany).

2.5. Cell culture conditions

The Ti6Al4V alloy samples used for cell culture experiments were disinfected in 70 % ethanol for 1 h and irradiated on each side with UV light for 30 min and inserted into 24-well plates (TPP, Switzerland). Human bone-marrow mesenchymal stromal cells (hBMSCs; 7500, ScienCell Research Laboratories, USA) were seeded onto the samples in a seeding density of 9000 cells per well (ca 5000 cells/cm^2) in 1 ml of α-MEM medium (Capricorn Scientific, Germany) supplemented with 15 % of fetal bovine serum (FBS), L-glutamine (2 mM; STA-B, Capricorn Scientific, Germany) and 1 % of antibiotic antimycotic solution (A5955; Sigma-Aldrich, USA). The cells were cultured in a humidified atmosphere at 37 °C and 5 % CO_2 for 21 days. After the initial 3 days of proliferation, the culture medium was enriched with 2-phospho-L-ascorbic acid (50 μM; 49752, Sigma-Aldrich, USA), β-glycerophosphate (20 mM; G9422, Sigma-Aldrich) and dexamethasone (10 nM; D2915, Sigma-Aldrich) to support osteogenic differentiation of the cells. The medium was replaced twice per week.

2.6. Resazurin assay

The metabolic activity of the mitochondrial enzymes of the hBMSC cells was evaluated by a resazurin assay. On days 1, 3, 7, 14, and 21 of cultivation, the samples were gently removed from the culture plates, washed with PBS and placed into fresh 24-well culture plates containing 1 ml of resazurin solution per well. The resazurin solution (40 μM) was prepared by adding resazurin (No. R7017, Sigma–Aldrich, USA) to the fresh phenol red-free culture medium supplemented with 10 % FBS. The plates were incubated at 37°C in a humidified atmosphere with 5 % CO_2, in darkness for 4 h (days 1 and 3), for 2 h (days 7 and 14) or for 1.5 h (day 21). After the incubation, the fluorescence intensity of the medium (150 μl in 3 parallel measurements) was measured (Ex/Em = 530/590 nm) using a Synergy HT Multi-Mode Microplate Reader (BioTek, USA) in triplicate aliquots. The resazurin solution without cells served as a blank control. Background fluorescence (from the blank) was subtracted, and the results were normalized to the number of cells per area of each sample.

2.7. Alkaline phosphatase activity assay

The osteogenic differentiation of the cells cultured on the samples

was evaluated by a quantitative assessment of alkaline phosphatase (ALP) enzymatic activity using 1-Step PNPP Substrate Solution (p-nitrophenyl phosphate; No. 37621, ThermoFisher Scientific) on days 7, 14, and 21 of culture. The samples were washed with PBS before analysis. Subsequently, 400 µL of PNPP solution was added to each sample, and the culture plates were incubated at room temperature (RT) and protected from light for 10 min. The absorbance of the resulting water-soluble yellow product was measured at 405 nm using a Synergy HT Multi-Mode Microplate Reader (BioTek, USA) in triplicate aliquots. The absorbance values were corrected to a blank control (PNPP solution without cells) and normalized to the number of cells per area of each sample.

2.8. Fluorescence staining and microscopy

Fluorescence staining was performed to visualize cell morphology on days 1 and 3, and the production of osteogenic markers (type I collagen, osteocalcin) by the cells on days 7, 14, and 21. After days 1 and 3 of cultivation, the samples were first rinsed with PBS and fixed using 4 % paraformaldehyde (pH 7.4) for 15 min, followed by two additional PBS washes. Fixed samples were then treated sequentially with 1 % bovine serum albumin in PBS containing 0.1 % of Triton X-100 for 20 min and with 1 % Tween 20 in PBS for another 20 min (both reagents from Sigma-Aldrich, USA). Cell nuclei were stained with Hoechst 33258 (5 µg/ml in PBS; Sigma-Aldrich; blue stain) while the F-actin cytoskeleton was stained with phalloidin-TRITC (100 ng/ml, red fluorescent signal; Sigma-Aldrich). All staining solutions were prepared in PBS and applied to the cells for 1 h at RT, protected from light. Microphotographs (10 per sample/well) were captured from randomly selected fields using an Olympus IX51 epifluorescence microscope paired with a DP74 camera (both from Olympus Corp., Japan). After days 7, 14, and 21 of cultivation, the cells were stained for type I collagen (all intervals) and osteocalcin (days 14 and 21), with the addition of Hoechst 33258 to stain cell nuclei. Briefly, the cells were fixed and treated by the same process as described above for blocking and permeabilization. Then, primary antibodies were applied, i.e., anti-type I collagen polyclonal antibody produced in rabbit (1:200, LSL-LB-1197 Cosmo Bio) at 4°C overnight for 7-day (7D) samples. For 14D and 21D samples, monoclonal anti-collagen type I antibody produced in mouse (1:200, C2456, Sigma-Aldrich, 3 h at RT) was applied, followed by rabbit anti-osteocalcin antibody (1:200, T-4743, Penninsula Laboratories) at 4°C overnight. Following that, secondary antibodies were applied for 90 min, i.e., Alexa Fluor™ 546 anti-Rabbit IgG (H+L) cross-adsorbed Secondary Antibody (A11010, Invitrogen, 1:400 for 7D), Alexa Fluor 546 Goat Anti-Mouse IgG (1:600 for 14D, 1:400 for 21D samples, A11003, Invitrogen), and Alexa Fluor 488 F(ab')2-Goat anti-Rabbit IgG (H+L) cross-adsorbed secondary antibody (1:600 for 14D samples and 1:400 for 21D, A-11070, Thermofisher Scientific). Cell nuclei were counterstained with Hoechst 33258 (5 µg/ml in PBS; Sigma-Aldrich) during incubation with secondary antibodies. Microphotographs were captured using a Leica Stellaris 8 inverted laser scanning confocal microscope (objective × 40, zoom 0.75). The numbers of cells growing on each sample at all observed time points were estimated from the Hoechst-stained cell nuclei. Image analysis was performed using ImageJ FIJI software (v. 1.54 f) [17] with the StarDist plugin [18] and Cellpose software v3.0.11. Representative images were selected for the figures.

2.9. Statistical analysis

Statistical analyses and visualization of data obtained in biological experiments were performed using GraphPad Prism 10 (GraphPad Software, USA). Two-Way ANOVA with Tukey's multiple comparisons test, or Kruskal-Wallis ANOVA with Dunn's test was applied depending on the data characteristics (normality, variance). The data are presented in summary graphs either as median with interquartile range (IQR) or mean with standard deviation (S.D.), which is specified in the respective figure captions. The significance of the differences was set at $p < 0.05$.

3. Results and discussion

3.1. Morphology and chemical analysis

The application of different surface pretreatment techniques resulted in statistically significant differences in surface textures in relation to R_a and R_z parameters ($p < 0.01$). Table 1 shows the evaluated roughness parameters Ra and Rz, which confirm that the application of MAO treatment significantly increased the roughness of polished, i.e., TAV(P)-Sr and TAV(P)-Sr-Ca surfaces. The surface roughness of the MAO coatings on blasted alloy, i.e., TAV(B)-Sr and TAV(B)-Sr-Ca, was similar to the unmodified TAV(B). Fig. 1 shows the surfaces treated by polishing (Fig. 1a) and blasting (Fig. 1d), including the hierarchical porous structures of MAO coatings (Fig. 1b, c, e, f). The different thicknesses of MAO coatings shown in Table 1 are related to the presence of Sr ions (conductivity 15.3 mS/cm) and a mixture of Sr and Ca ions (conductivity 17.9 mS/cm) with other ions H^+, OH^-, Na^+, $PO_4^{3-}CH_3COO^-$. A greater thickness of MAO coatings was prepared in electrolytes containing Sr and Ca ions, which corresponds to a higher plasma discharge intensity at the substrate-electrolyte interface. The different state of the microstructure of the surface prepared by TAV(B) blasting reaches an irregular character (Fig. 1d) with open spaces in which air can be trapped, and the surface wettability decreased (i.e., contact angle increased) [19]. The samples that were polished and subsequently treated with MAO showed a reduction in contact angle (CA) and an increase in surface hydrophilicity (Table 1).

The cross-sections of the MAO coatings are shown in Fig. 2 with the identification of the elements present (P, Ti, O, Sr, Ca). The evolution of the layer thickness and porous structure of MAO coatings is accompanied by electrochemical, chemical, and thermal reactions. When the desired voltage is reached, dielectric breakdown and oxide layer growth occur, accompanied by a decrease in current and condensation of oxides of key elements contained in the electrolyte. Based on the elemental mapping results (Fig. 2), it can be concluded that the elements are present throughout the thickness of the coating. In addition to the pores that are present, microcracks can also be observed in the cross-section of the coatings, which occur due to thermal stresses during rapid solidification of the molten oxide in the electrolyte [7].

The crystalline phases of the MAO coatings were characterized by X-ray diffraction (XRD), with representative patterns for each sample presented in Fig. 3. The micro-arc oxidation process predominantly leads to the formation of titanium dioxide in the anatase phase. As reported in the literature [19,20], the localized high temperatures (>800 °C) and plasma discharges at the oxide layer–electrolyte interface induce partial transformation of anatase into the thermodynamically stable rutile phase [21]. Rapid cooling may also lead to the formation of an amorphous phase, as indicated by the presence of Sr.

Table 1
Surface roughness, thickness and surface wettability of samples.

Sample	Roughness (µm)		MAO-coating (µm)	Surface wettability (°)
	R_a	R_z	Layer	CA
TAV(P)	0.21 ± 0.01	1.90 ± 0.19	-	71.23 ± 5.72
TAV(B)	3.62 ± 0.35	22.53 ± 3.96	-	129.80 ± 5.44
TAV(P)-Sr	1.49 ± 0.12	9.98 ± 0.94	9.49 ± 0.78	48.10 ± 8.36
TAV(B)-Sr	3.76 ± 0.26	22.16 ± 1.65	7.95 ± 0.73	46.20 ± 9.66
TAV(P)-Sr-Ca	1.80 ± 0.07	11.87 ± 0.69	16.16 ± 1.00	49.44 ± 7.45
TAV(B)-Sr-Ca	3.77 ± 0.55	25.93 ± 0.77	14.63 ± 1.27	49.20 ± 5.45

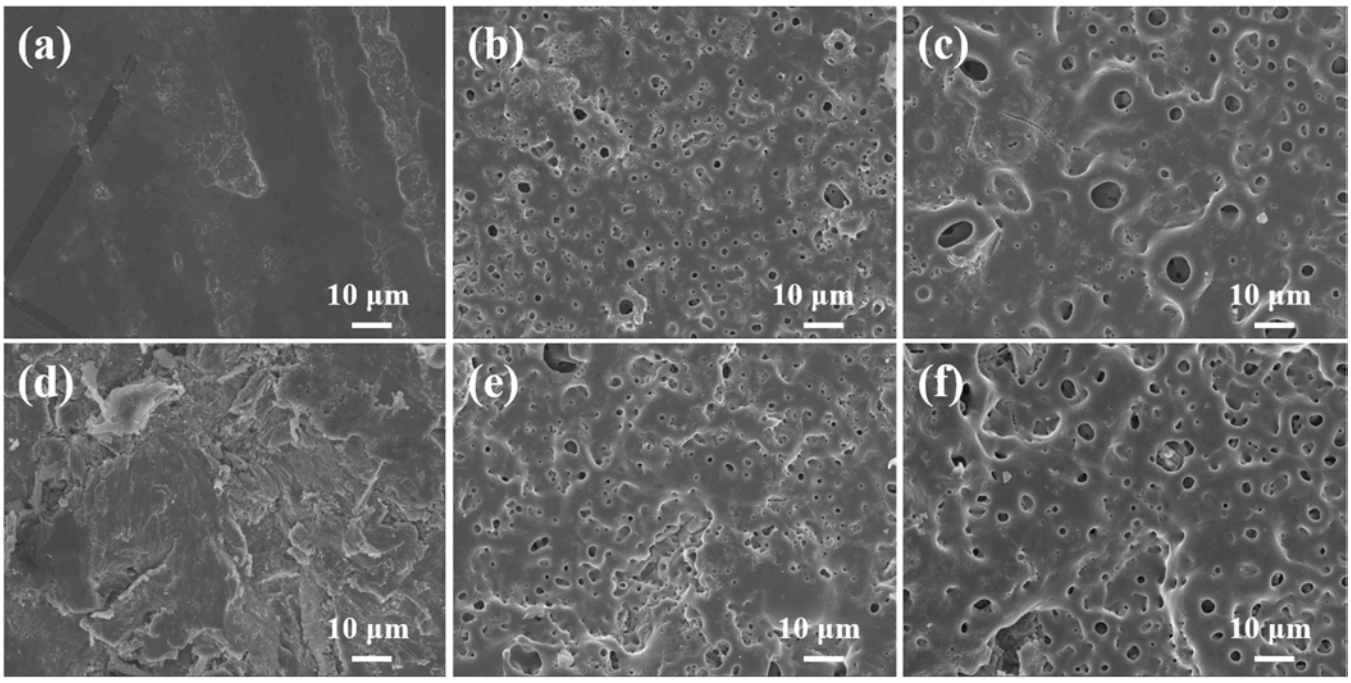

Fig. 1. Surface SEM images of TAV(P) (a); TAV(P)-Sr (b); TAV(P)-Sr-Ca (c); TAV(B) (d); TAV(B)-Sr (e); TAV(B)-Sr-Ca (f).

The presence of the Al_2O_3 phase was detected in the XRD patterns of the TAV(B)-Sr-Ca and TAV(B)-Sr coatings, corresponding to the alumina used in the blasting medium. Diffraction peaks corresponding to metallic Ti originate from X-ray penetration through the coating, revealing contributions from the underlying substrate. The heterogeneity of the coating composition and variations in surface morphology affect the intensity and resolution of the detected phases.

Depending on the substrate composition and the ionic species present in the electrolyte, certain oxide systems remain amorphous, whereas crystalline phases form locally during the micro-arc discharge. To complement the XRD analysis and achieve detailed identification of the oxide systems, X-ray photoelectron spectroscopy (XPS) was employed.

$$Ti - 4e \rightarrow Ti^{4+} \quad (1)$$

$$4H_2O + 4e \rightarrow 4OH^- + 2H_2 \quad (2)$$

$$Ti^{4+} + 2OH^- \rightarrow TiO_2 + 2H^+ \quad (3)$$

The results of the calculated atomic concentrations are shown in Table 2 and Supplementary Table S1. The results do not include concentrations of carbon, which is considered only as a contaminant.

For the individual XPS spectra of the elements (Fig. 4), a charging correction was made during the measurements (a shift on the energy scale) so that the position of the carbon emission line corresponds to graphitic carbon and, at the same time, the position of the main Ti 2p peak is at 458.8 eV. The value of the Ti binding energy and the shape of the Ti 2p spectrum correspond to the presence of TiO_2 oxide on the sample surface. The photoemission peak O 1 s in Fig. 4 is similar for all samples. The main peak at a binding energy of 531 eV seems to correspond to a mixture of TiO_2 and other oxides present. It is impossible to distinguish the individual contributions due to their similar binding energy. The mixture of different contributions corresponds to the relatively large width of this peak. Other peaks at higher binding energies are due to surface contamination by hydrocarbons.

In Fig. 4, the spectra of Sr 3d and P 2p are shown, where there is a significant overlap. These lines represent the main peaks of Sr and P. In order to perform the deconvolution, additional peaks of both elements, i.e., Sr 3p and P 2s, were measured. The position of Sr at a binding energy of 133.4 eV indicates the likely presence of SrO oxide.

The Ca 2p photoemission spectrum with a maximum binding energy of 347.3 eV was observed for the TAV(P)-Sr-Ca and TAV(B)-Sr-Ca samples (Fig. 4). Due to the nibbling effect, the binding energy value is significantly shifted and may correspond to the presence of a compound in the form of $Ca_3(PO_4)_2$ [20] or CaO [21], in accordance with the electrolyte composition of the MAO process. According to a study by Zhang et. al. [22], the Ca^{2+}, Na^+ and Sr^{2+} ions in the electrolyte can react with OH^- and PO_4^{3-} ions to form Sr-and Na- bound co-substituted hydroxyapatite (SNH) coatings (Eq. 4).

$$(10-x-y)Ca^{2+} + xSr^{2+} yNa^+ + 6PO_4^{3-} + 4OH^- \rightarrow Ca_{10-x-y}Sr_yNa_y(PO_4)_6(OH)_2 \quad (4)$$

3.2. Wear behavior

Among all tested coatings, the TAV(B)-Sr surface exhibited the most favorable tribological performance, characterized by the lowest and most stable coefficient of friction together with a minimal wear rate (Fig. 5). The dominant abrasive wear mechanism was confirmed by the morphology of both the wear track and the worn ball surface (Fig. 6), indicating that the Sr-modified MAO layer on blasted substrates provides a mechanically robust surface capable of resisting friction-induced degradation. In contrast, the TAV(P)-Sr coating showed the highest and markedly unstable coefficient of friction, which corresponded with progressive penetration through the outer porous MAO layer and subsequently through the denser inner layer until the Ti6Al4V substrate was exposed. This observation was corroborated by EDX point analysis (Fig. 7), where the chemical composition inside the wear track closely matched that of the underlying alloy, confirming complete coating failure in the most heavily loaded regions. The combined adhesive–abrasive wear mechanism observed on TAV(P)-Sr further reflects insufficient mechanical stability of the porous outer layer on polished substrates.

Adhesion testing provided additional insight into coating integrity. The TAV(P)-Sr-Ca coating demonstrated excellent cohesion and

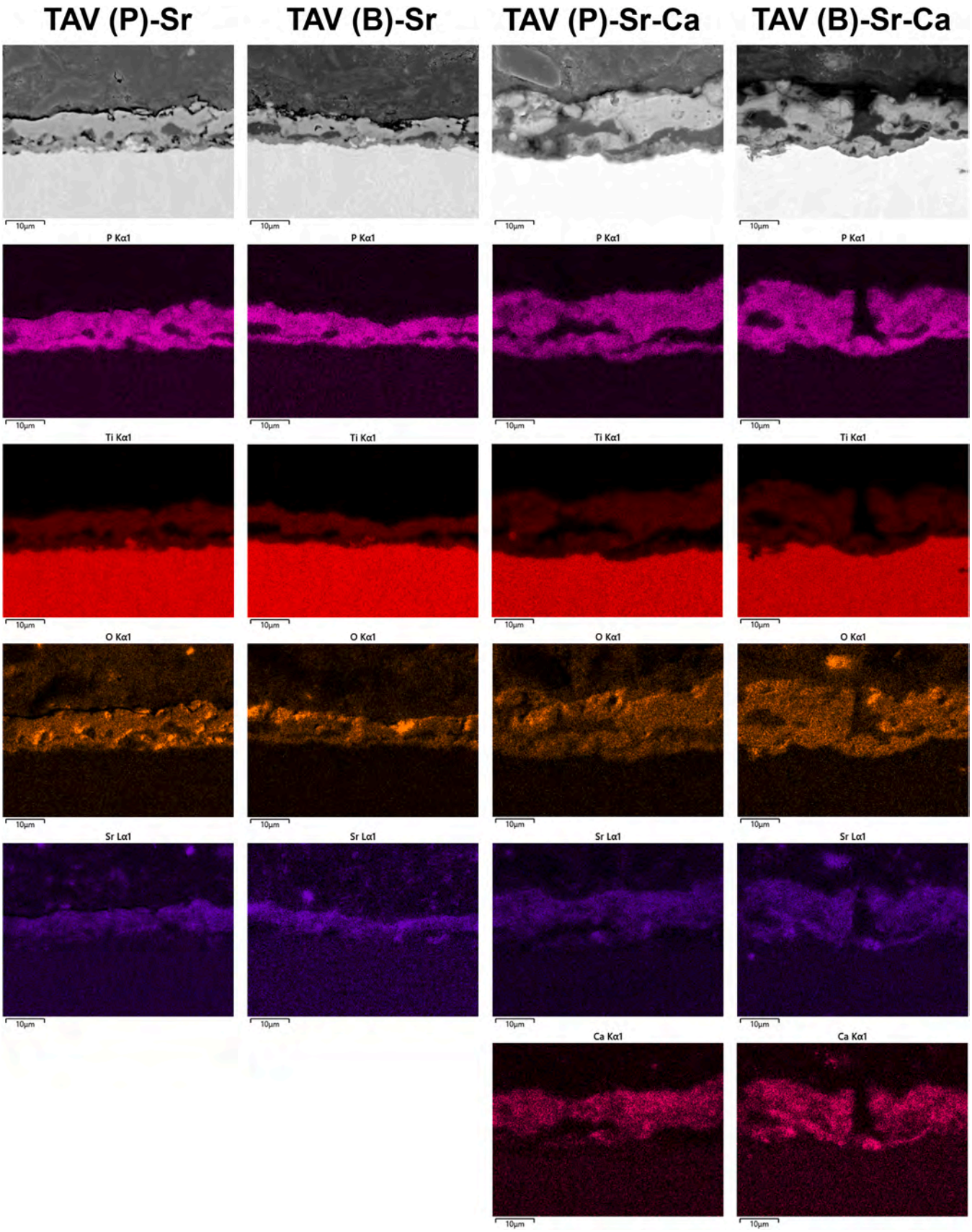

Fig. 2. EDX elemental mapping.

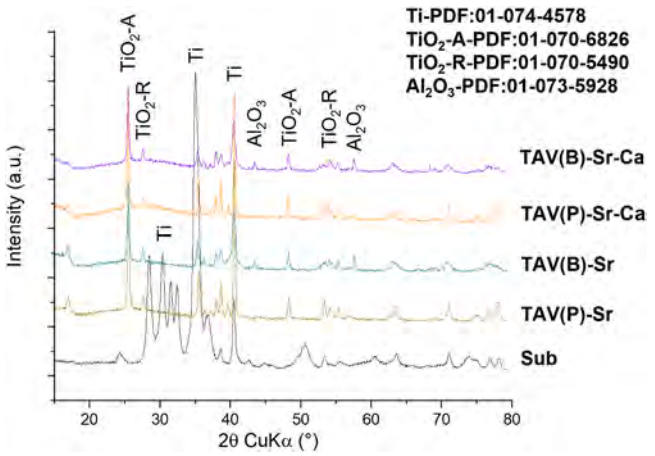

Fig. 3. XRD patterns of Ti6Al4V (TAV) modified with blasting (B), grinding and polishing (P), and MAO coatings.

Table 2
XPS analysis of the MAO coatings (wt%).

Sample	Element (in wt%)						
	Ti	O	Na	Ca	P	Sr	C
TAV (P)-Sr	14.7	27.9	1.4	-	22.9	27.5	5.8
TAV (P)-Sr-Ca	13.2	30.2	0.9	8.7	17.8	16.4	12.8
TAV (B)-Sr	7.8	29.5	1.9	-	19.9	24.0	16.9
TAV (B)-Sr-Ca	11.6	30.9	1.1	7.4	21.1	18.3	9.6

adhesion, remaining intact without delamination even at the maximum applied load of 30 N (Fig. 8a), indicating strong bonding both within the MAO layers and at the coating–substrate interface. In contrast, the TAV (P)-Sr coating exhibited initial delamination of the outer coating at a critical load of 17.5 N (Fig. 8b), suggesting weaker bonding between the outer and inner MAO layers. Nevertheless, the inner MAO layer maintained full adhesion to the substrate up to 30 N, indicating that optimization of MAO processing parameters could mitigate the interlayer instability observed in the TAV(P)-Sr system.

3.3. Corrosion resistance and ion release

The corrosion resistance of MAO coatings in the corrosive environment of the isotonic physiological solution was determined by potentiodynamic polarization curves (Fig. 9). Table 4 shows the calculated values of corrosion potential (E_{cor}) and corrosion current density (J_C) based on the Tafel extrapolation method. The shift of E_{cor} towards positive values for the polished MAO coatings TAV(P)-Sr and TAV(P)-Sr-Ca indicates that these MAO surfaces are less reactive to corrosive environments. The shift of the corrosion potential toward more positive values indicates improved thermodynamic stability of the surface, while the increased corrosion current density suggests that the protective capability of the coating is limited primarily due to its porous structure.

The potentiodynamic polarization curves (Fig. 9) reveal distinct electrochemical behavior for each sample. TAV(P) exhibited the lowest J_c (0.095 μA/cm^2) and a highly negative E_{cor} (-551.8 mV vs. SCE), suggesting a strong passive oxide layer and high corrosion resistance. This aligns with findings that polished Ti6Al4V maintains better passivity due to a compact oxide film [23]. TAV(B) showed increased J_c (0.239 μA/cm^2) and a less negative E_{cor} (-222.5 mV), indicating higher susceptibility to corrosion. Shot-blasting introduces surface defects, leading to a weaker protective oxide layer and higher dissolution rates [24]. After MAO modification, TAV(P)-Sr and TAV(P)-Sr-Ca displayed significantly shifted E_{cor} towards more noble values (-25.6 mV and 188.6 mV, respectively), but also higher J_c (0.508 and 0.770 μA/cm^2). This suggests that Sr and Ca incorporation reduces the thermodynamic tendency for corrosion, and results in a more porous oxide structure that increases localized degradation [25]. For blasted samples, TAV(B)-Sr and TAV(B)-Sr-Ca exhibited the highest J_c (1.410 and 2.629 μA/cm^2) and the most negative E_{cor} (-536.0 mV and −685.9 mV, respectively).

The Bode impedance plots (Fig. 10a) provide insight into the frequency-dependent behavior of the coatings. The TAV(P) sample exhibited the highest impedance values across all frequencies, indicating superior corrosion resistance due to the formation of a dense, less porous oxide layer. This observation is consistent with previous findings, where polished Ti6Al4V demonstrated improved corrosion resistance due to the formation of a more uniform and compact passive film [25]. In contrast, the TAV(B) sample displayed the lowest impedance values, particularly at low frequencies, suggesting higher electrolyte penetration and weaker barrier properties. Shot-blasting introduces

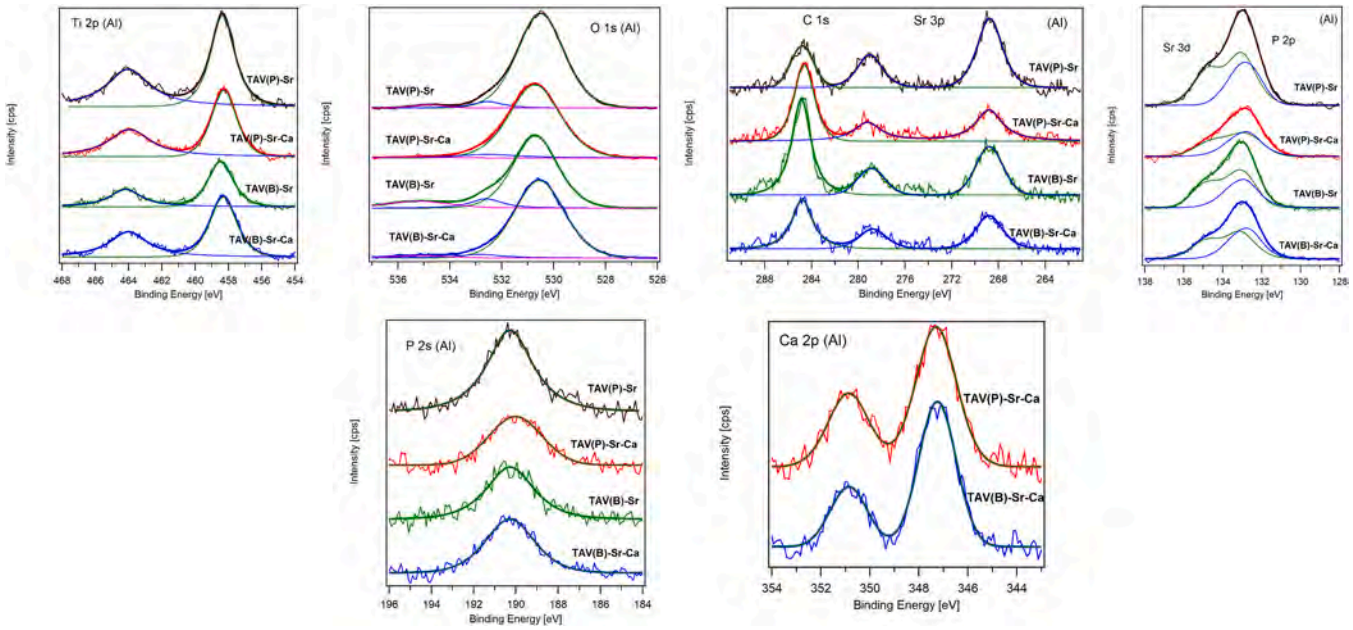

Fig. 4. XPS spectra of MAO coatings.

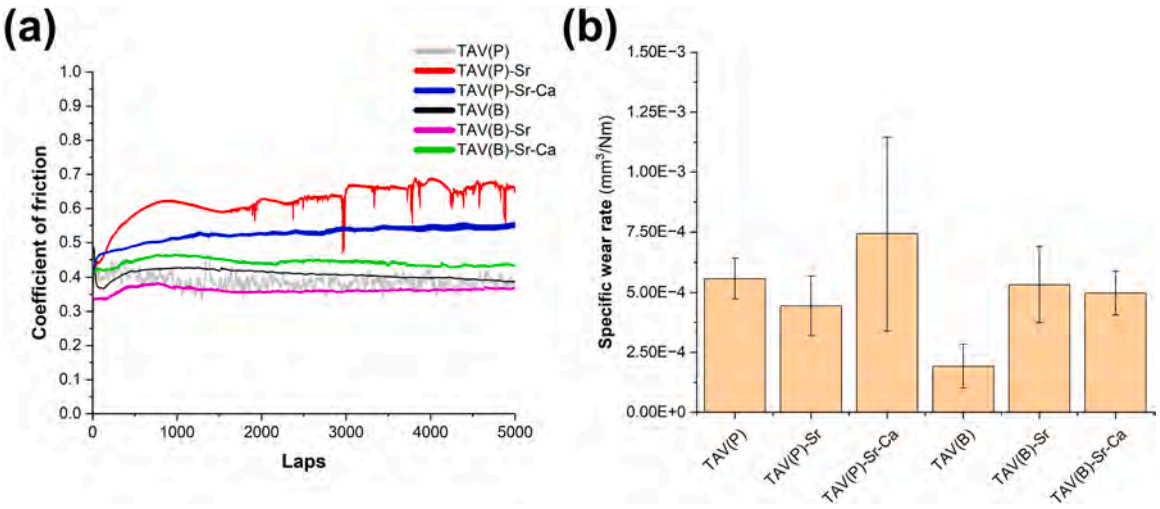

Fig. 5. Tribology test: (a) course of the friction coefficient and (b) wear rate.

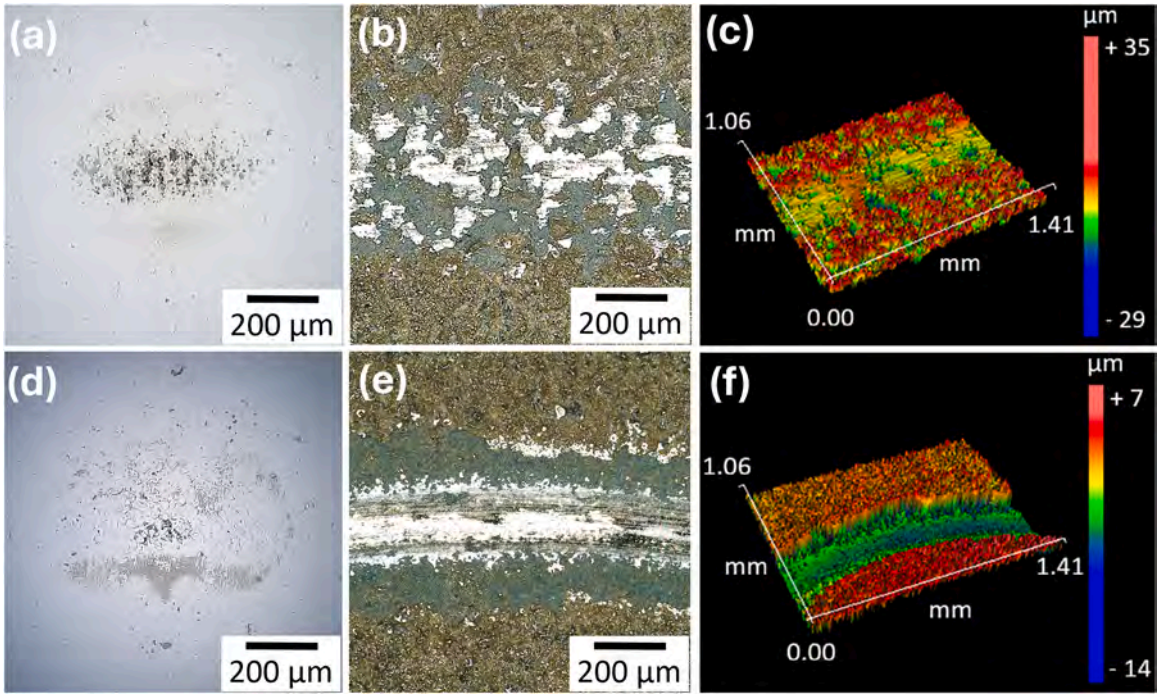

Fig. 6. Wear of friction pairs after the tribological tests in PBS solution. TAV(B)-Sr coating: (a) Al_2O_3 ball, (b) wear track, (c) wear track profile. TAV(P)-Sr coating: (d) Al_2O_3 ball, (e) wear track, and (f) wear track profile.

microstructural defects and increased surface roughness, which can lead to a reduction in charge transfer resistance and overall impedance [26].

The incorporation of Sr and Ca via MAO treatment significantly improved the impedance values compared to the untreated samples. TAV(P)-Sr and TAV(P)-Sr-Ca samples exhibited higher impedance than TAV(P), indicating that Sr and Ca enhance the protective oxide layer, making it more resistant to electrolyte penetration. Previous studies have shown that Sr-containing MAO coatings increase corrosion resistance by forming stable Sr-phosphate compounds, which contribute to improved barrier properties. Similarly, Ca incorporation has been reported to enhance oxide layer stability and reduce capacitance, thereby improving corrosion resistance [25]. For the shot-blasted samples, TAV (B)-Sr and TAV(B)-Sr-Ca demonstrated moderate impedance improvement compared to TAV(B), suggesting that the MAO treatment can partially counteract the negative effects of shot-blasting. However, the impedance values remained lower than those of the polished samples, indicating that the initial surface roughness still influences the overall electrochemical behavior.

The Nyquist plots (Fig. 10b) further support the Bode plot findings by illustrating the charge transfer resistance (Rct) of each sample. The TAV (P) sample exhibited the largest semicircle, confirming its superior corrosion resistance due to a well-formed, protective oxide layer. This trend is consistent with previous literature, where larger semicircles in Nyquist plots correspond to higher Rct values and improved corrosion protection [25].

Following MAO treatment, the Nyquist response improved significantly for TAV(P)-Sr and TAV(P)-Sr-Ca, indicating enhanced charge transfer resistance and lower corrosion rates. This enhancement is attributed to the formation of Sr- and Ca-containing compounds within the oxide layer, which contribute to a denser, more protective coating.

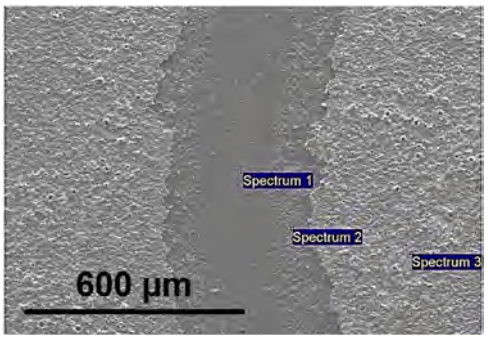

Fig. 7. EDX point chemical analysis of TAV(P)-Sr wear track: Spectrum 1 – Ti6Al4V substrate, Spectrum 2 – inner MAO layer, and Spectrum 3 – outer MAO layer.

Table 3
EDX analysis of the chemical composition of the TAV (P)-Sr sample at the tested points of the friction track. Data are expressed as mean±SD (wt%).

Spectrum	O	Al	Ti	V	Sr	P
1	28.5 ± 0.3	3.5 ± 0.2	63.8 ± 0.1	2.6 ± 0.2	-	1.3 ± 0.2
2	54.8 ± 0.2	2.6 ± 0.2	29.8 ± 0.1	0.8 ± 0.2	-	11.8 ± 0.1
3	43.6 ± 0.3	2.5 ± 0.2	38.0 ± 0.1	1.2 ± 0.2	2.1 ± 0.3	12.3 ± 0.1

Fig. 8. Scratch test of (a) TAV (P)-Sr-Ca and (b) TAV (P)-Sr coatings. Load from 1 N to 30 N on a 3 mm scratch length.

The incorporation of Sr in particular has been shown to promote the formation of Sr-phosphates, which improve adhesion and barrier properties [25]. Conversely, TAV(B) showed the smallest semicircle, confirming the negative impact of shot-blasting on corrosion resistance. The introduction of roughness and microstructural defects accelerates the charge transfer processes, leading to faster corrosion kinetics [26]. However, TAV(B)-Sr and TAV(B)-Sr-Ca exhibited an increase in semicircle size, indicating that MAO modification improves corrosion resistance even in shot-blasted samples, though not to the same extent as polished ones.

The release of Sr ions was performed under PBS solution conditions at pH 7.4, which did not change during the analysis at each sampling interval (1, 7, 14, 28, 60 days). The changes in the concentration of Sr released into the PBS solution and the calculated fractions of Sr from the total contents from each MAO coating are shown in Fig. 11. Strontium oxide, which has been proven in the layer, reacts with water and therefore its solubility is related to the solubility of strontium hydroxide, which is formed by a reaction with water. At 20 °C the solubility of Sr $(OH)_2$ is up to 7 g per litre. The dissolution of SrO under PBS solution conditions is affected by their ions and the solubility of the formed Sr $(OH)_2$ may be different from that in pure water (Eq. 5). The results show that there is an increase in the determined Sr content in the solution over the time interval studied. After 60 days, more than 25 wt% Sr was released from the total Sr content in all the MAO coatings studied.

$$SrO + H_2O \rightarrow Sr(OH)_2 \quad (5)$$

3.4. Cell adhesion, proliferation and differentiation

The human bone marrow mesenchymal stromal cells (hBMSCs) were seeded onto the prepared samples and cultivated for 21 days, during which they were analyzed in predetermined time intervals. On day 1 after seeding, the number of initially adhered cells was similar on all surfaces. The substrate material modified only with grinding and polishing, i.e. TAV(P) sample, supported cell spreading better than the other samples, as is illustrated by the cell morphology after 1 day of cultivation (Fig. 12a). The cells on TAV(P) were more elongated with longer protrusions and a rich actin filament cytoskeleton. The TAV(P) surface was significantly smoother than all other samples, as is apparent from the roughness parameters (Table 1). The contact angle of approximately 71.2° indicated a moderate wettability of the material surface, contributing to improved cell spreading and uniform, mostly elongated morphology of all attached cells. Cells on the other samples spread less uniformly across the sample surface, and more often exhibited polygonal morphology. Especially among the cells on the blasted samples, i.e., TAV(B) group, a more compact, rounded morphology and long, thin protrusions were observed. The differences in cell morphology are a direct reaction of the cells trying to accommodate to the more rugged surface topography (Table 2, Fig. 1). An effect of Sr, Ca, and P ions, dissolved from MAO-treated surfaces, on the cell morphology is also possible, even on day 1, as shown in Fig. 11. In addition, we observed improved metabolic activity of hBMSC on both TAV(P) and TAV(P)-Sr compared to all other samples on day 1. In a study by Zhang et al. [27], the initial cell adhesion of MC3T3-E1 cells on porous Sr/Ag-containing TiO_2 coatings, prepared by MAO, was highest on the surfaces with a Sr/Ag ratio of 19.3/0 wt% and decreased with increased Ag content, reaching a minimum at a Sr/Ag ratio of 14.85/1.25 wt% one and two hours after seeding. On day 1, a decrease in cell proliferation was observed in these samples from the Sr/Ag content of 18.73/0.26 wt %. The increased Ag content was accompanied by a decrease in O content, which may have influenced the initial cell attachment. Our MAO-modified samples contained Sr in the range of 16.4–27.5 wt%, corresponding to 5.9–9.9 at% (Tables 2, S1), and the cells proliferated on all samples for 21 days.

The number of cells growing on the samples after 3 days showed that the TAV(P) samples promoted an increase in cell proliferation (Fig. 12b). A similar effect was seen in the increased cell metabolic activity, normalized per cell, on the TAV(P) samples, which reached the highest levels of all the samples, together with TAV(P)-Sr samples on day 3. In general, the samples with the lowest relative surface roughness and porosity, i.e. TAV(P) and TAV(P)-Sr, appeared to promote faster cell proliferation. Among the blasted sample group, the highest metabolic activity was observed in TAV(B) (Fig. 12c). After 3 days of cultivation, the proliferation culture medium was changed to the medium supporting osteogenic cell differentiation. On day 7, the TAV(P) and TAV(P)-Sr samples, where the cells reached the highest population densities, exhibited a notable reduction in metabolic activity. Conversely, on samples with lower cell population densities, the cells became more metabolically active (Fig. 12d).

During the following week, the cells on all samples reached confluence, and their proliferation rate was lower, except for the TAV(B)-Sr-Ca sample, on which the cell number exceeded the value on the other samples on day 14 of cultivation (Fig. 12b). This is in accordance with a recent study by Li et al. [28] who observed that Sr^{2+} ions supported stem cell asymmetric division and stem cell renewal, preserved a high number of cells in S-phase and thus enhanced proliferation in the early stage of osteogenic induction both *in vitro* and *in vivo*.

In a study by Zhang et al. [10] MC3T3-E1 preosteoblasts exhibited higher metabolic activity when grown on strontium-containing

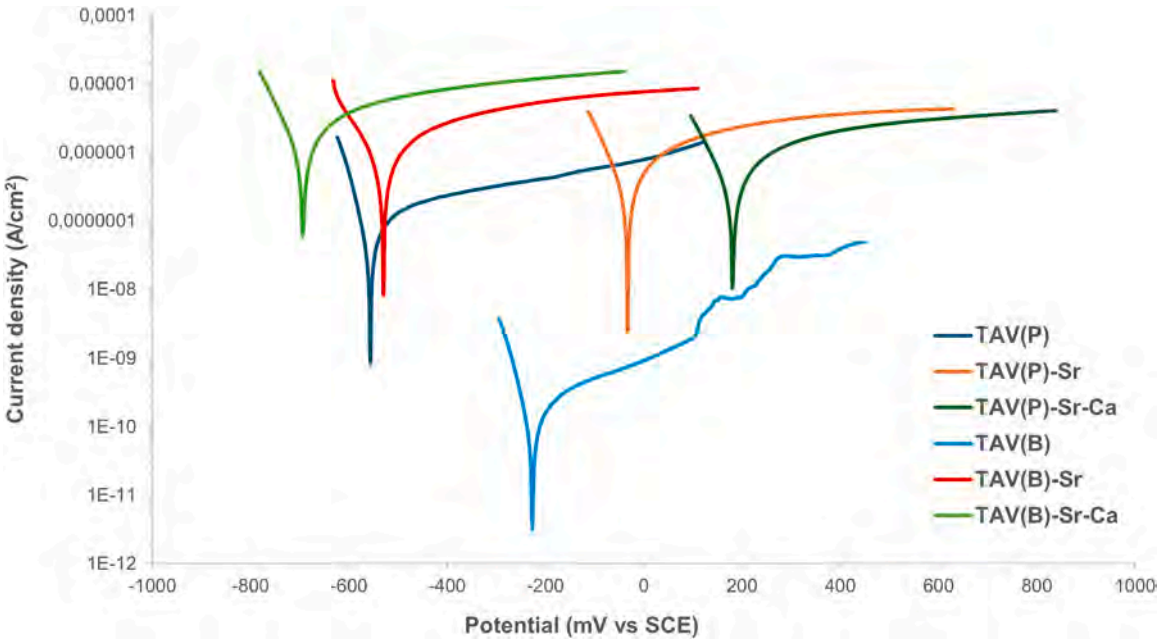

Fig. 9. Electrochemical corrosion behavior.

Table 4
Corrosion parameters of the studied samples obtained by the Tafel method.

Sample	Corrosion potential E_{cor} (mV vs. SCE)	Corrosion current density J_C ($\mu A/cm^2$)
TAV (P)	-551.8	0.095
TAV (P)-Sr	-25.6	0.508
TAV (P)-Sr-Ca	188.6	0.770
TAV (B)	-222.5	0.239
TAV (B)-Sr	-536.0	1.410
TAV (B)-Sr-Ca	-685.9	2.629

hydroxyapatite layers developed by MAO technique on Ti6Al4V on days 3 and 7 of culture. This activity increased proportionally to the Sr content, which was in the range from 0.86 to 5.4 at%. The highest value is similar to that of our MAO-modified TAV samples, with Sr content ranging from 5.9 to 9.9 at%, i.e. from 16.4 to 27.5 wt%.

On day 21, the cells growing on all samples reached similar population densities. However, significantly higher metabolic activity was observed in cells on the TAV(B)-Sr sample compared to both TAV(P) and TAV(P)-Sr samples (Fig. 12d). The TAV(B)-Sr sample released Sr into PBS in moderate concentrations over long time intervals (Fig. 11), which could support the cell metabolism.

On day 7, there was a significant increase in metabolic activity that matched the changes in ALP activity, which is a marker of early and mid-term osteogenic cell differentiation. This increase was observed in cells on samples modified with both Sr and Ca, in both the polished and blasted groups, i.e., TAV(P)-Sr-Ca and TAV(B)-Sr-Ca, which were closely followed by samples modified only with Sr, i.e., TAV(P)-Sr and TAV(B)-Sr. From a biological point of view, the effect on early osteogenic differentiation of hBMSCs represented by analysis of ALP activity on day 7 was high, as the increase in ALP activity was ~ 4-fold between TAV(P) and TAV(P)-Sr-Ca, and nearly 3-fold between TAV(B) and TAV(B)-Sr-Ca. The maximum values of ALP activity of the cells *in vitro* are usually detected between day 7 and 10, followed by a decrease to certain lower values. The date demonstrated the earliest onset of the osteogenic cell differentiation on both TAV(B)-Sr-Ca and TAV(P)-Sr-Ca (Fig. 12e), which is a prerequisite for rapid bone regeneration and can significantly shorten the healing time in patients. On day 14, the ALP activity reached relatively similar levels in all samples, with the highest value recorded in the TAV(B) group. This suggests either a delayed or, rather, a weaker but prolonged, positive effect of TAV(B) on osteogenic cell differentiation compared to the other samples in the blasted group. This effect

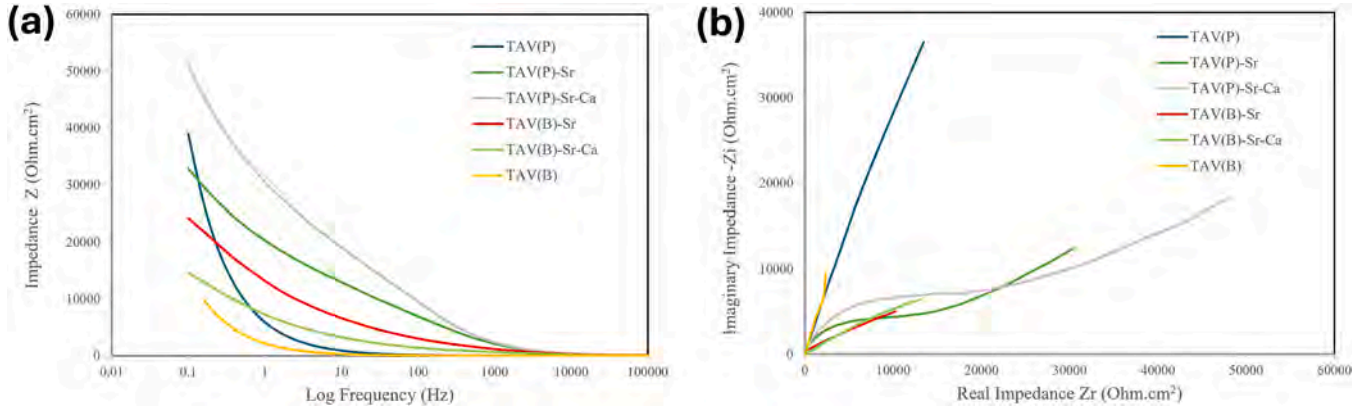

Fig. 10. (a) Bode and (b) Nyquist diagrams.

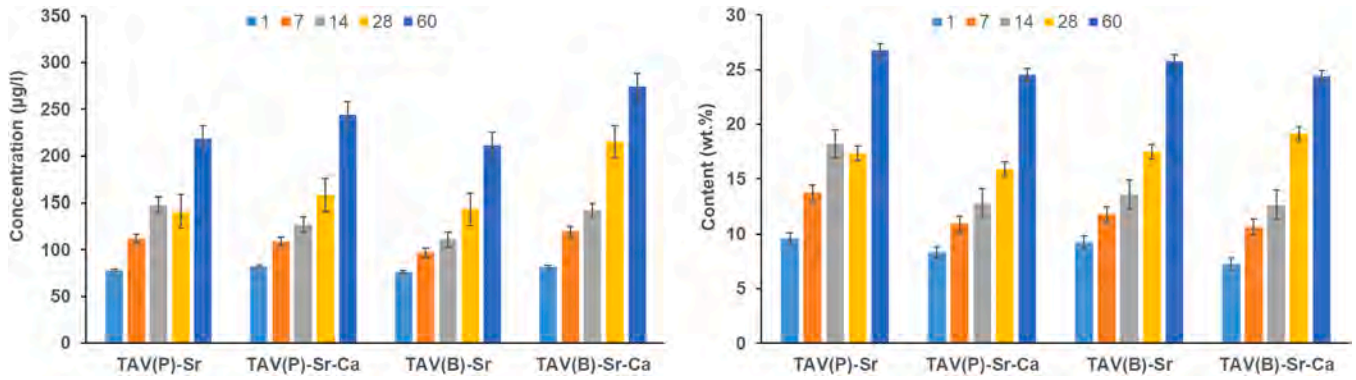

Fig. 11. Determination of Sr stability in MAO coatings in SBF solution (1, 7, 14, 28, and 60 days). All experiments and measurements were performed in four replicates; the results are represented by mean ± standard deviation (S.D.).

diminished but remained still observable on day 21.

The supportive effect of Sr-Ca modification on the early osteogenic differentiation is also indicated by the higher cellular production and deposition of type I collagen on the sample surface on day 7. Significantly higher collagen deposition per single cell was observed on TAV (P)-Sr-Ca samples compared to all other samples except for TAV(B)-Sr-Ca (Fig. 13a,b). A gradually increasing but similar deposition of type I collagen and osteocalcin was observed on all tested samples by confocal microscopy on days 14 and 21 (Supplementary Fig. S1). On day 21, the mature, correctly assembled collagen fibers were present on all samples, as documented by SHG imaging (Supplementary Fig. S2). The collagen fibers visualized on the blasted sample group appear less bright due to their prominent topography. This topography penetrates the layers of the extracellular matrix deposited by the cells, so the fibers could not be fully distinguished when the maximum projection was created from the z-stack image.

Due to their similar structures, calcium and strontium both act as agonists to calcium-sensing receptors, which are expressed on the surface of precursor cells, such as bone marrow mesenchymal stromal cells (BMSC), or differentiated cells, including osteoblasts and osteoclasts [29,30]. The effects of Sr and Ca are mediated through the activation of multiple intracellular signaling pathways that regulate cell behavior in terms of survival, proliferation, and differentiation. For example, activating the PI3K/AKT and the canonical Wnt/β-catenin pathways in osteoblasts leads to the upregulation of genes related to osteogenic differentiation (e.g., alkaline phosphatase, osteocalcin, type I collagen). Stroncium can also inhibit the formation and differentiation of bone-resorbing osteoclast cells and promote the apoptosis of mature osteoclasts by activating DAG-PKC βII and other pathways (for a review, see [31]). In our experiments, we observed a positive effect of Sr on early osteogenic differentiation, evidenced by notably higher alkaline phosphatase activity and increased type I collagen deposition by hBMSCs growing for 7 days on the samples modified with Sr and Ca (Fig. 12e, Fig. 13).

The long-term release of Sr from the samples was highest for TAV(B)-Sr-Ca, followed by TAV(P)-Sr-Ca and the other samples. The sustained release of Sr is important for the long-term bioactivity of implants. EDX analysis of the MAO coatings after the 21-day incubation with cells (Table 5) showed relatively high concentrations of Sr and P, and an average Ca concentration on the TAV(P)-Sr-Ca sample. Interestingly, the TAV(P)-Sr samples contained as many Ca ions as the MAO coatings with Sr and Ca. This suggests significant deposition of Ca by the hBMSCs on this sample. On the other hand, TAV (B)-Sr contained lower concentrations of Ca on its surface, although the P and Sr concentrations were similar to those of most of the samples. The precipitation/dissolution of hydroxyapatite and the relative incorporation of Sr into hydroxyapatite seemed to differ in the tested samples. The surface created by MAO modification with both Ca and Sr ions more closely simulated natural conditions for hydroxyapatite precipitation.

Zhou et al. [32] studied the osteogenic potential of Ti coatings doped with Ca, P, Co and F, with different Sr contents, i.e. 6, 11, and 18 wt%, prepared by MAO. RT-PCR analysis of rabbit bone marrow MSCs cultured on these layers showed increased expression of the genes involved in osteogenesis, such as runt-related transcription factor 2 (runx2), osteocalcin, bone sialoprotein, type I collagen, and osteopontin on all MAO-treated samples compared to control Ti during 14-day cell culture. Increasing the Sr content further stimulated all these genes, reaching a maximum level at 15 wt% Sr. *In vivo* implantation of Ti implants coated with the same layers in the femoral shafts of rabbits for 8 weeks also showed enhanced osseointegration, as measured by bone-to-implant contact rate and a pull-out force. The highest values were observed for the Sr content of 11 wt%, with values gradually decreasing for 18, 6 and 0 wt%.

There are also water molecules present within the apatite crystal and on its surface, creating a hydrated layer with an amorphous calcium phosphate-like phase [8], which may contain a variety of ions and charged proteins. The mineral ions present in the hydrated layer may be incorporated into the regular, non-stoichiometric apatite crystals during their growth [33]. Conversely, nanocrystalline apatites can act as reservoirs of mineral ions, which are slowly released either spontaneously through reverse ion exchange with calcium ions in body fluids in the surrounding environment, or through the complete dissolution of the apatite crystals by osteoclasts. The former process of ion release could predominantly be involved in the local stimulation of stem cells or osteoblasts on Ca-P (Sr) nanocrystalline materials and other ceramics, as well as in their interaction with tissues [33].

Strontium is rapidly incorporated into newly formed bone regions. Cooper et al. [34] proved the presence of higher concentrations of Sr in the periosteal lamellae and in the trabecular remodeling sites of the vertebrae of rats treated with strontium ranelate. Li et al. [35] quantified the incorporation of Sr into newly-formed bone and discovered that Sr replaced around 3–5 % of Ca within the apatite crystal lattice. During the treatment of osteoporosis in postmenopausal women, the administration of 2 g/day of strontium ranelate resulted in around 5 % of Ca replacement by Sr in the lattice of newly formed bone apatite [35]. In a study performed on dogs, Frankær et al. [36] found that 35–45 % of Sr was present in the highly ordered sites of the hydroxyapatite, 5–35 % of Sr was found on the surface of the apatite crystals or collagen, and a significant proportion (30–50 %) of Sr was present in bone fluids. Modifying the hydroxyapatite crystals with 10 % Sr changed their properties, making them smaller and more soluble; the apatite crystals also contained more CO_3 in their lattice.

Pure titanium implants with a surface that was sandblasted and acid-etched were implanted into the proximal tibias of rats [37]. The animals treated with strontium ranelate showed improvement in bone microarchitecture around the implant, as well as increased pull-out strength, elastic modulus, tissue hardness, and working energy of the cortical bone near the implants, compared to the untreated control group.

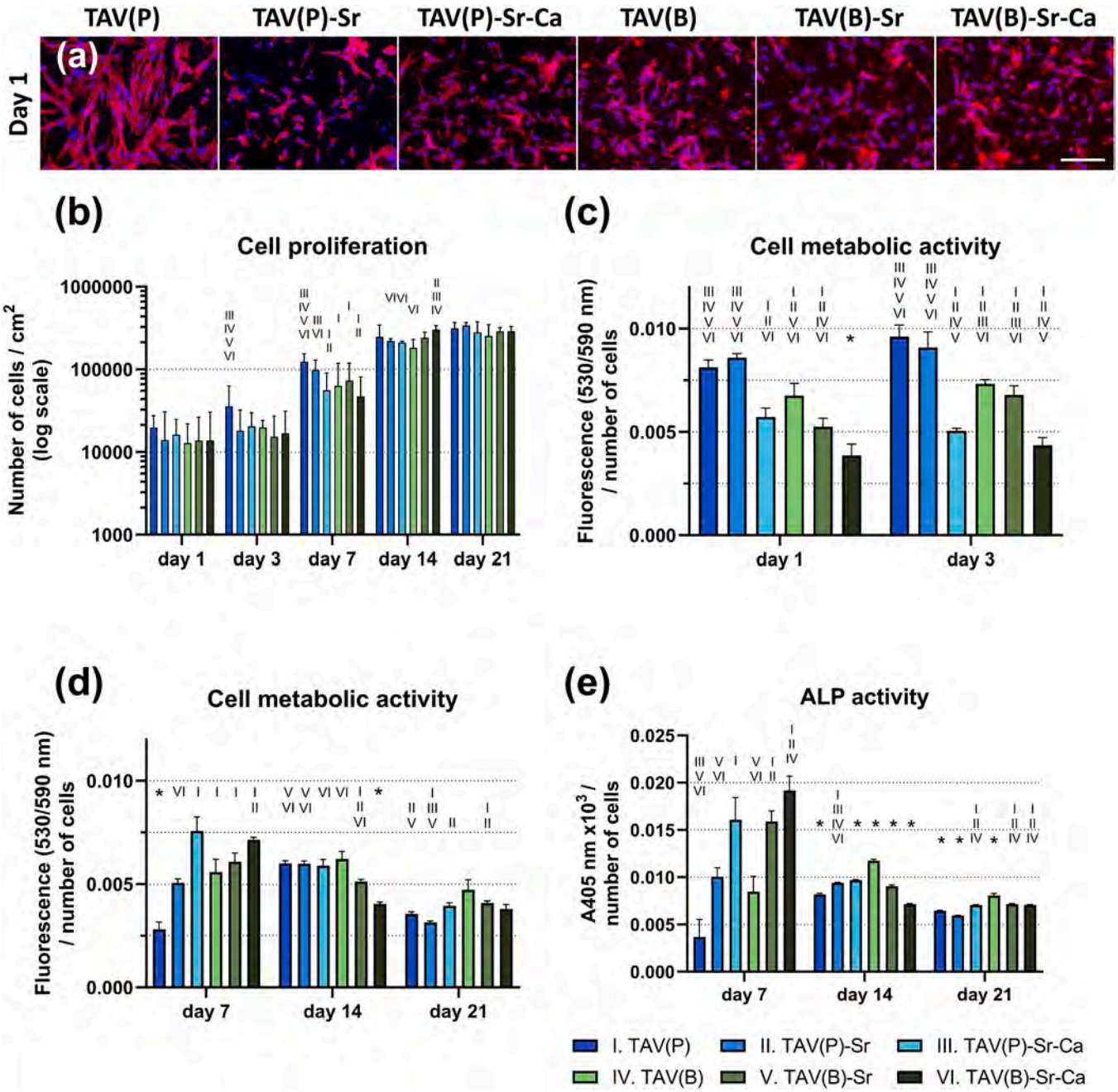

Fig. 12. Proliferation and differentiation of hBMSC on the material surface. **(a)** Cell morphology on day 1 visualized by fluorescent staining of the cell nuclei (blue fluorescence) and F-actin filaments of the cell cytoskeleton (red fluorescence). Olympus IX51, DP74 camera, objective × 10, scale bar = 200 μm. **(b)** Proliferation of hBMSC on the materials. The data are expressed as median with IQR; n = 20–30 (day 1 and 3), n = 16 (day 7), n = 8 (day 14 and 21). **(c)** Cell metabolic activity measured on days 1 and 3, and **(d)** on days 7, 14, and 21 after seeding. Mean with S.D., n = 3. **(e)** Differentiation of hBMSC cells on the materials was measured as the enzymatic activity of alkaline phosphatase (ALP). Mean with S.D., n = 3. Two-Way ANOVA with Tukey's multiple comparisons test, or Kruskall-Wallis ANOVA with Dunn's test, was applied depending on the data ($p < 0.05$). Comparisons were made for each time interval separately; * means significance against all samples.

However, some studies have not proven the positive effect of Sr doping on implant osseointegration. The *in vivo* implantation of cylindrical Ti6Al4V implants coated with 5 % Sr-doped hydroxyapatite into dog bones did not affect implant fixation or osseointegration compared to HA-coated implants after 4 and 12 weeks. When Sr-doped hydroxyapatite was mixed with an allograft and implanted as a bone graft extender, increased bone formation (by 21 %) and allograft preservation (by 18 %) were observed, but the newly-formed bone was not in direct contact with the implant [38]. In these studies, however, the long-term release of Sr was not evaluated.

4. Conclusions

We prepared polished or blasted Ti6Al4V samples, i.e. TAV(P) and TAV(B) samples of different surface roughness, which were further modified using the MAO technique. The MAO treatment resulted in the creation of TAV(P)-Sr, TAV(P)-Sr-Ca, TAV(B)-Sr and TAV(B)-Sr-Ca surfaces. The physical and chemical properties, as well as the biocompatibility of the prepared samples were then analyzed.

The presence of Sr, P, and Ca in the prepared ceramic coatings was confirmed by EDX and XPS analyses. The Sr ions were released continuously from the samples for 60 days. TAV(B)-Sr and TAV(B)-Sr-Ca

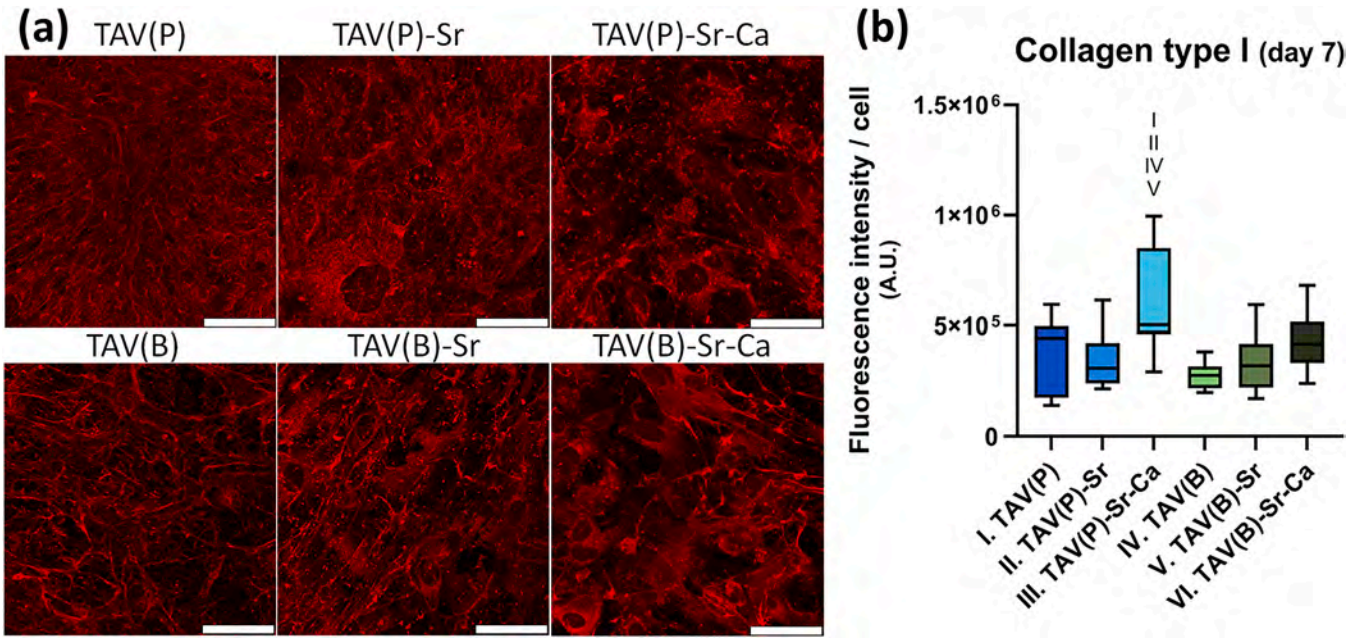

Fig. 13. Immunofluorescence staining of type I collagen (a) and fluorescence intensity of collagen after staining (b) on day 7 of cultivation. (a) Leica Stellaris 8 confocal microscope, objective × 40, zoom × 1.5, scale bar = 100 μm. (b) Box plot (median, minimum and maximum values, and IQR), n = 8. Two-Way ANOVA with Tukey's multiple comparisons test ($p < 0.05$).

Table 5
EDX analysis of the MAO coatings (wt%) with cells after 21 days of cell cultivation.

Sample	Element (in wt%)							
	C	O	Ti	Ca	P	Sr	Al	V
TAV (P)-Sr	53.5 ± 0.4	29.3 ± 0.4	7.8 ± 0.1	4.5 ± 0.1	3.8 ± 0.1	0.8 ± 0.1	0.3 ± 0.1	-
TAV (P)-Sr-Ca	10.3 ± 0.6	52.5 ± 0.5	21.9 ± 0.3	4.1 ± 0.1	5.9 ± 0.1	3.0 ± 0.1	1.3 ± 0.1	1.0 ± 0.1
TAV (B)-Sr	48.6 ± 0.4	33.1 ± 0.4	11.0 ± 0.1	1.3 ± 0.1	2.9 ± 0.1	1.3 ± 0.1	1.4 ± 0.1	0.4 ± 0.1
TAV (B)-Sr-Ca	47.2 ± 0.4	34.5 ± 0.4	7.5 ± 0.1	4.9 ± 0.1	3.5 ± 0.1	1.1 ± 0.1	0.9 ± 0.1	0.4 ± 0.1

coating layers exhibited higher Ra and Rz roughness values than TAV (P)-Sr and TAV(P)-Sr-Ca surfaces. Thicker coatings were produced on the samples with Sr-Ca doping.

The MAO process enabled the creation of an abrasion-resistant surface. The analysis of wear resistance revealed an increasing coefficient of friction as follows: TAV(B)-Sr coating < TAV(P) < TAV(B) < TAV(B)-Sr-Ca < < TAV(P)-Sr-Ca < TAV(P)-Sr.

The results describing the corrosion behavior of MAO indicated a significant effect of surface pretreatment, particularly due to surface defects introduced by blasting. The incorporation of Sr and Ca ions into the electrolyte contributed to the formation of a stable MAO oxide layer and enhanced the surface bioactivity.

In vitro experiments with human bone marrow stromal cells (hBMSCs) showed the excellent biocompatibility of all the prepared surface layers. The supportive effect of Sr and Sr-Ca modification on early osteogenic cell differentiation was documented by an increase in alkaline phosphatase activity and type I collagen deposition, which was prominent on both polished TAV(P) and shot-blasted TAV(B) samples.

CRediT authorship contribution statement

Jana Seidlerova: Writing – review & editing, Supervision, Funding acquisition. **Ladislav Cvrcek:** Writing – original draft, Visualization, Methodology, Investigation, Formal analysis. **Elena Filova:** Writing – original draft, Visualization, Methodology, Investigation, Formal analysis, Conceptualization. **Michaela Tokarcíkova:** Visualization, Methodology, Investigation, Formal analysis. **Roman Gabor:** Writing – original draft, Visualization, Project administration, Methodology, Investigation, Funding acquisition, Formal analysis, Conceptualization. **Lucie Bacakova:** Writing – review & editing, Supervision, Funding acquisition. **Martina Doubkova:** Writing – original draft, Visualization, Methodology, Investigation, Formal analysis, Conceptualization. **Josef Hlinka:** Writing – original draft, Visualization, Methodology, Investigation, Funding acquisition, Formal analysis. **Grazyna Simha Martynkova:** Writing – review & editing, Visualization, Methodology, Investigation, Formal analysis. **Marina Malic:** Writing – review & editing, Visualization, Investigation, Formal analysis. **Karel Masek:** Writing – original draft, Visualization, Methodology, Investigation, Formal analysis. **Jan Walter:** Methodology, Investigation, Formal analysis. **Marek Vecer:** Visualization, Methodology, Formal analysis.

Declaration of Competing Interest

The authors declare that they have no known competing financial interests or personal relationships that could have appeared to influence the work reported in this paper.

Acknowledgments

This paper was created as part of the project No. CZ.02.01.01/00/22_008/0004631 "Materials and technologies for sustainable development" (MATUR) within the Jan Amos Komensky Operational Program of the Ministry of Education, Youth and Sports of the Czech Republic, co-funded by the European Union. Further support was provided by the Czech Academy of Sciences (*Praemium Academiae* grant No. AP2202). The authors also thank Mrs. Ivana Zajanova (Institute of Physiology,

Czech Academy of Sciences, Prague) for her assistance with the immunofluorescence staining.

Appendix A. Supporting information

Supplementary data associated with this article can be found in the online version at doi:10.1016/j.colsurfa.2025.139438.

Data Availability

According to the Open Science principles, the data presented in this study will be available at doi: zenodo.org/uploads/15279524, and are also available on request from the corresponding author.

References

[1] M.Z. Ibrahim, A.A.D. Sarhan, F. Yusuf, M. Hamdi, Biomedical materials and techniques to improve the tribological, mechanical and biomedical properties of orthopedic implants – A review article, J. Alloy. Compd. 714 (2017) 636–667, https://doi.org/10.1016/j.jallcom.2017.04.231.

[2] N. Kohli, J.C. Stoddart, R.J. van Arkel, The limit of tolerable micromotion for implant osseointegration: a systematic review, Sci. Rep. 11 (1) (2021) 10797, https://doi.org/10.1038/s41598-021-90142-5.

[3] G.C. Cardoso, C.R. Grandini, J.V. Rau, Comprehensive review of PEO coatings on titanium alloys for biomedical implants, J. Mater. Res. Technol. 31 (2024) 311–328, https://doi.org/10.1016/j.jmrt.2024.06.068.

[4] Z. Lin, T. Wang, X. Yu, X. Sun, H. Yang, Functionalization treatment of micro-arc oxidation coatings on magnesium alloys: a review, J. Alloy. Compd. 879 (2021) 160453, https://doi.org/10.1016/j.jallcom.2021.160453.

[5] J. Yang, K. Fang, K. Xu, X. Shen, X. Xu, Effect of zinc or copper doping on corrosion resistance and anti-oxidative stress of strontium-based micro-arc oxidation coatings on titanium, Appl. Surf. Sci. 626 (2023) 157229, https://doi.org/10.1016/j.apsusc.2023.157229.

[6] R. Gabor, L. Cvrček, S. Causidu, K. Drobikova, M. Večeř, K.M. Kutláková, M. Buřil, J. Hlinka, J. Seidlerová, Effect of additive for preparation of reduced-porosity ceramic layer on Ti-6Al-4 V alloy for orthopaedic and trauma implants, Surf. Interfaces 25 (2021) 101209, https://doi.org/10.1016/j.surfin.2021.101209.

[7] Y. Wang, F. Ba, Z. Chai, Z. Zhang, A review of thermal control coatings prepared by micro-arc oxidation on light alloys, Int. J. Electrochem. Sci. 19 (3) (2024) 100514, https://doi.org/10.1016/j.ijoes.2024.100514.

[8] W. Querido, A.L. Rossi, M. Farina, The effects of strontium on bone mineral: A review on current knowledge and microanalytical approaches, Micron 80 (2016) 122–134, https://doi.org/10.1016/j.micron.2015.10.006.

[9] E. Bonnelye, A. Chabadel, F. Saltel, P. Jurdic, Dual effect of strontium ranelate: stimulation of osteoblast differentiation and inhibition of osteoclast formation and resorption in vitro, Bone 42 (1) (2008) 129–138, https://doi.org/10.1016/j.bone.2007.08.043.

[10] Z.-Y. Zhang, T.-Y. Huang, D.-J. Zhai, H.-B. Wang, K.-Q. Feng, L. Xiang, Study on strontium doped bioactive coatings on titanium alloys surfaces by micro-arc oxidation, Surf. Coat. Tech. 451 (2022) 129045, https://doi.org/10.1016/j.surfcoat.2022.129045.

[11] J. Shi, Y. Li, Y. Gu, S. Qiao, X. Zhang, H. Lai, Effect of titanium implants with strontium incorporation on bone apposition in animal models: a systematic review and meta-analysis, Sci. Rep. 7 (1) (2017) 15563, https://doi.org/10.1038/s41598-017-15488-1.

[12] X. Shen, K. Fang, K.H. Ru Yie, Z. Zhou, Y. Shen, S. Wu, Y. Zhu, Z. Deng, P. Ma, J. Ma, J. Liu, High proportion strontium-doped micro-arc oxidation coatings enhance early osseointegration of titanium in osteoporosis by anti-oxidative stress pathway, Bioact. Mater. 10 (2022) 405–419, https://doi.org/10.1016/j.bioactmat.2021.08.031.

[13] X. Yang, Q. Wang, C. Yan, D. Huang, Y. Zhang, H. He, S. Xiong, C. Li, P. Chen, T. Ye, D. Hu, L. Wang, A dual-functional strontium-decorated titanium implants that guides the immune response for osseointegration of osteoporotic rats, Colloids Surf. B. 233 (2024) 113643, https://doi.org/10.1016/j.colsurfb.2023.113643.

[14] K. Zhou, M. Wang, S. Zhang, J. Huo, W. Zheng, M.R.I. Abueida, Q. Wang, H. Liu, Z. Yi, Titanium alloys for orthopedic applications: a review on the osteointegration induced by physicomechanical stimuli, J. Mater. Res. Technol. 30 (2024) 8260–8276, https://doi.org/10.1016/j.jmrt.2024.05.207.

[15] G. Mendonça, D.B.S. Mendonça, F.J.L. Aragão, L.F. Cooper, Advancing dental implant surface technology – From micron- to nanotopography, Biomaterials 29 (28) (2008) 3822–3835, https://doi.org/10.1016/j.biomaterials.2008.05.012.

[16] R. Gabor, I. Šlamborová, K. Mašek, M. Večeř, G. Simha Martynková, J. Hlinka, M. Tokarčíková, O. Motyka, P. Běčák, J. Seidlerová, Structural modification of aluminium alloy for preparation of hydrophobic and antibacterial ZnO-based coatings, Ceram. Int. 50 (18, Part B) (2024) 33751–33761, https://doi.org/10.1016/j.ceramint.2024.06.193.

[17] J.R. Moffitt, D. Bambah-Mukku, S.W. Eichhorn, E. Vaughn, K. Shekhar, J.D. Perez, N.D. Rubinstein, J. Hao, A. Regev, C. Dulac, X. Zhuang, Molecular, spatial, and functional single-cell profiling of the hypothalamic preoptic region, Science 362 (6416) (2018), https://doi.org/10.1126/science.aau5324.

[18] U. Schmidt, M. Weigert, C. Broaddus, G. Myers, Cell Detection with Star-Convex Polygons, in: A.F. Frangi, J.A. Schnabel, C. Davatzikos, C. Alberola-López, G. Fichtinger (Eds.), Medical Image Computing and Computer Assisted Intervention – MICCAI 2018, Springer International Publishing, Cham, 2018, pp. 265–273.

[19] K.J. Kubiak, M.C.T. Wilson, T.G. Mathia, P. Carval, Wettability versus roughness of engineering surfaces, Wear 271 (3) (2011) 523–528, https://doi.org/10.1016/j.wear.2010.03.029.

[20] J. Han, P. Wan, Y. Ge, X. Fan, L. Tan, J. Li, K. Yang, Tailoring the degradation and biological response of a magnesium–strontium alloy for potential bone substitute application, Mater. Sci. Eng. C. 58 (2016) 799–811, https://doi.org/10.1016/j.msec.2015.09.057.

[21] Y. Li, W. Wang, F. Yu, D. Wang, S. Guan, Y. Li, M. Qi, Characterization and cytocompatibility of hierarchical porous TiO2 coatings incorporated with calcium and strontium by one-step micro-arc oxidation, Mater. Sci. Eng. C. 109 (2020) 110610, https://doi.org/10.1016/j.msec.2019.110610.

[22] L. Zhang, H. Li, K. Li, Y. Zhang, S. Liu, Q. Guo, S. Li, Micro-oxidation treatment to improve bonding strength of Sr and Na co-substituted hydroxyapatite coatings for carbon/carbon composites, Appl. Surf. Sci. 378 (2016) 136–141, https://doi.org/10.1016/j.apsusc.2016.03.216.

[23] N. Sharma, R. Kamparath, S. Pal, C. Mukherjee, N.S. Benerji, Grain-wise piezoelectric response of polycrystalline aluminum nitride thin films: an empirical investigation using piezo force microscopy, J. Phys. D Appl. Phys. 58 (4) (2025) 045302, https://doi.org/10.1088/1361-6463/ad8897.

[24] B.M. Gillespie, R.M. Walker, E. McInnes, Z. Moore, A.M. Eskes, T. O'Connor, E. Harbeck, C. White, I.A. Scott, H. Vermeulen, W. Chaboyer, Preoperative and postoperative recommendations to surgical wound care interventions: a systematic meta-review of Cochrane reviews, Int. J. Nurs. Stud. 102 (2020) 103486, https://doi.org/10.1016/j.ijnurstu.2019.103486.

[25] J. Han, P. Wan, Y. Sun, Z. Liu, X. Fan, L. Tan, K. Yang, Fabrication and evaluation of a bioactive Sr–Ca–P contained micro-arc oxidation coating on magnesium strontium alloy for bone repair application, J. Mater. Sci. Technol. 32 (3) (2016) 233–244, https://doi.org/10.1016/j.jmst.2015.11.012.

[26] P. Ebrahimzadeh, L.B. Peral, R. González-Martínez, E. Mardaras, I. Fernández-Pariente, Influence of severe surface plastic deformation induced by shot peening on microstructure and corrosion resistance of fine grained 316 L stainless steel, Corros. Sci. 231 (2024) 111988, https://doi.org/10.1016/j.corsci.2024.111988.

[27] Y.Y. Zhang, Y. Zhu, D.Z. Lu, W. Dong, W.J. Bi, X.J. Feng, L.M. Wen, H. Sun, M. C. Qi, Evaluation of osteogenic and antibacterial properties of strontium/silver-containing porous TiO(2) coatings prepared by micro-arc oxidation, J. Biomed. Mater. Res. B Appl. Biomater. 109 (4) (2021) 505–516, https://doi.org/10.1002/jbm.b.34719.

[28] Y. Li, J. Yue, Y. Liu, J. Wu, M. Guan, D. Chen, H. Pan, X. Zhao, W.W. Lu, Strontium regulates stem cell fate during osteogenic differentiation through asymmetric cell division, Acta Biomater. 119 (2021) 432–443, https://doi.org/10.1016/j.actbio.2020.10.030.

[29] R. Mentaverri, S. Yano, N. Chattopadhyay, L. Petit, O. Kifor, S. Kamel, E. F. Terwilliger, M. Brazier, E.M. Brown, The calcium sensing receptor is directly involved in both osteoclast differentiation and apoptosis, Faseb J. 20 (14) (2006) 2562–2564, https://doi.org/10.1096/fj.06-6304fje.

[30] H. Cho, J. Lee, S. Jang, J. Lee, T.I. Oh, Y. Son, E. Lee, CaSR-Mediated hBMSCs activity modulation: additional coupling mechanism in bone remodeling compartment, Int. J. Mol. Sci. 22 (1) (2021) 325, https://doi.org/10.3390/ijms22010325.

[31] B. Kołodziejska, N. Stępień, J. Kolmas, The influence of strontium on bone tissue metabolism and its application in osteoporosis treatment, Int. J. Mol. Sci. 22 (12) (2021) 6564, https://doi.org/10.3390/ijms22126564.

[32] J. Zhou, X. Wang, L. Zhao, Antibacterial, angiogenic, and osteogenic activities of Ca, P, Co, F, and Sr compound doped titania coatings with different Sr content, Sci. Rep. 9 (1) (2019) 14203, https://doi.org/10.1038/s41598-019-50496-3.

[33] S. Cazalbou, D. Eichert, X. Ranz, C. Drouet, C. Combes, M.F. Harmand, C. Rey, Ion exchanges in apatites for biomedical application, J. Mater. Sci. Mater. Med. 16 (5) (2005) 405–409, https://doi.org/10.1007/s10856-005-6979-2.

[34] D.M. Cooper, L.D. Chapman, Y. Carter, Y. Wu, A. Panahifar, H.M. Britz, B. Bewer, W. Zhouping, M.J. Duke, M. Doschak, Three dimensional mapping of strontium in bone by dual energy K-edge subtraction imaging, Phys. Med. Biol. 57 (18) (2012) 5777–5786, https://doi.org/10.1088/0031-9155/57/18/5777.

[35] C. Li, O. Paris, S. Siegel, P. Roschger, E.P. Paschalis, K. Klaushofer, P. Fratzl, Strontium is incorporated into mineral crystals only in newly formed bone during strontium ranelate treatment, J. Bone Miner. Res. 25 (5) (2010) 968–975, https://doi.org/10.1359/jbmr.091038.

[36] C.G. Frankær, A.C. Raffalt, K. Stahl, Strontium localization in bone tissue studied by X-ray absorption spectroscopy, Calcif. Tissue Int 94 (2) (2014) 248–257, https://doi.org/10.1007/s00223-013-9806-7.

[37] L. Maïmoun, T.C. Brennan, I. Badoud, V. Dubois-Ferriere, R. Rizzoli, P. Ammann, Strontium ranelate improves implant osseointegration, Bone 46 (5) (2010) 1436–1441, https://doi.org/10.1016/j.bone.2010.01.379.

[38] M.T. Vestermark, Strontium in the bone-implant interface, Dan. Med. Bull. 58 (5) (2011) B4286.